Organic molecular dynamics and charge-carrier lifetime in lead iodide perovskite MAPbI$_3$

Akihiro Koda[a,b], Hirotaka Okabe[a], Masatoshi Hiraishi[a], Ryosuke Kadono[a,b,1] ![ORCID], Katelyn A. Dagnall[c] ![ORCID], Joshua J. Choi[c], and Seung-Hun Lee[d,1] ![ORCID]

[a]Muon Science Laboratory and Condensed Matter Research Center, Institute of Materials Structure Science, High Energy Accelerator Research Organization (KEK), Tsukuba, Ibaraki 305-0801, Japan; [b]Department of Materials Structure Science, The Graduate University for Advanced Studies, Tsukuba, Ibaraki 305-0801, Japan; [c]Department of Chemical Engineering, University of Virginia, Charlottesville, VA 22904; and [d]Department of Physics, University of Virginia, Charlottesville, VA 22904

The long charge carrier lifetime of the hybrid organic–inorganic perovskites (HOIPs) is the key for their remarkable performance as a solar cell material. The microscopic mechanism for the long lifetime is still in debate. Here, by using a muon spin relaxation technique that probes the fluctuation of local magnetic fields, we show that the muon depolarization rate (Δ) of a prototype HOIP methylammonium lead iodide (MAPbI$_3$) shows a sharp decrease with increasing temperature in two steps above 120 K and 190 K across the structural transition from orthorhombic to tetragonal structure at 162 K. Our analysis shows that the reduction of Δ is quantitatively in agreement with the expected behavior due to the rapid development of methyl ammonium (MA) jumping rotation around the C_3 and C_4 symmetry axes. Our results provide direct evidence for the intimate relation between the rotation of the electric dipoles of MA molecules and the charge carrier lifetime in HOIPs.

organic–inorganic hybrid perovskite | carrier lifetime | cation dynamics | muon spin rotation

Hybrid organic-inorganic perovskites (HOIPs) have been attracting enormous research interest as one of the most promising materials for the next-generation solar cells that combine high efficiency and low cost (1). The power-conversion efficiency (PCE) of HOIP-based solar cells has reached above 25% (2), which is comparable to that of silicon solar cells. In view of the social implementation, the merit is emphasized that HOIP solar cells can be manufactured by using simple solution processing methods with drastically low costs compared with the current commercial solar cell technologies. Meanwhile, the most promising HOIP family including the prototype methylammonium lead iodide (MAPbI$_3$, where MA denotes CH$_3$NH$_3^+$) has been shown to be chemically unstable (3), and the attempts to replace Pb with less toxic elements have had limited success in achieving high PCE (4, 5). Moreover, the microscopic mechanism of the high PCE in the MAPbI$_3$ family is still elusive, despite years of extensive research on their basic properties.

One of the most important properties relevant to the high photovoltaic performance of HOIPs is their long carrier lifetimes ($\gtrsim 1\ \mu$s) observed in thin films, which translates to large carrier diffusion lengths, despite their modest charge mobilities (6). Several microscopic mechanisms behind the unusually long carrier lifetime have been proposed, such as the formation of ferroelectric domains (7–9), the Rashba effect (10, 11), the photon recycling (12), and the formation of large polarons (13, 14). When the HOIPs are replaced with all inorganic perovskites in the photovoltaic architecture, the device can still function as a solar cell. This indicates that the photons excite electrons and holes out of the inorganic metal halide atoms, which is consistent with the density functional theory (DFT) calculations that the corner interstitial cations, whether organic or inorganic, do not directly contribute to the band-edge states. However, the lower efficiency of the purely inorganic perovskites suggests that the presence of organic cation may be the key for achieving high PCE, although the microscopic details on how the organic cations enhance the efficiency is unclear at this stage.

The crystal structure of HOIP is represented by that of MAPbI$_3$ consisting of the three-dimensional network of corner-shared PbI$_6$-octahedra and CH$_3$NH$_3^+$ molecule ions at the A site in the generic perovskite structure ABO_3, where the orthorhombic structure ($Pnma$) observed at low temperatures is shown in Fig. 1. There is now a consensus in the community that the long carrier lifetime is mainly due to the formation of large polarons (13, 14). The screened carriers are protected from scattering by defects and phonons, leading to the prolonged carrier lifetime (13–16). The possibility of large polaron formation (13, 14) by the reorientation of organic cations in response to the presence of photoexcited carriers (15, 16) is of particular interest in view of the cation molecular dynamics; the screened carriers are protected from scattering by defects and phonons, leading to the prolonged lifetime (13, 14, 16). The microscopic mechanism of the screening must be associated with both lattice vibrations (13, 14) and molecular rotations (15, 16) in response to the presence of photoexcited carriers. It is still an open question how much contribution each of the two make for the screening in HOIPs. Figuring out their contributions quantitatively is important because it will guide us in searching

---

Significance

Hybrid organic–inorganic perovskites (HOIPs) are among the most promising materials for next-generation solar cells that combine high efficiency and low cost. The record efficiency of HOIP-based solar cells has reached above 25%, and they can be manufactured using simple solution-processing methods that can be drastically cheaper than the current commercial solar cell technologies. Despite the progress so far, the microscopic mechanism for the high solar cell efficiency in HOIPs is yet to be understood. In this study, we show that the ability of organic molecules to rotate on an appropriate time scale in HOIPs can extend the lifetime of photoexcited charge carriers and lead to higher efficiency. This insight can guide the progress toward improved solar cell performance.
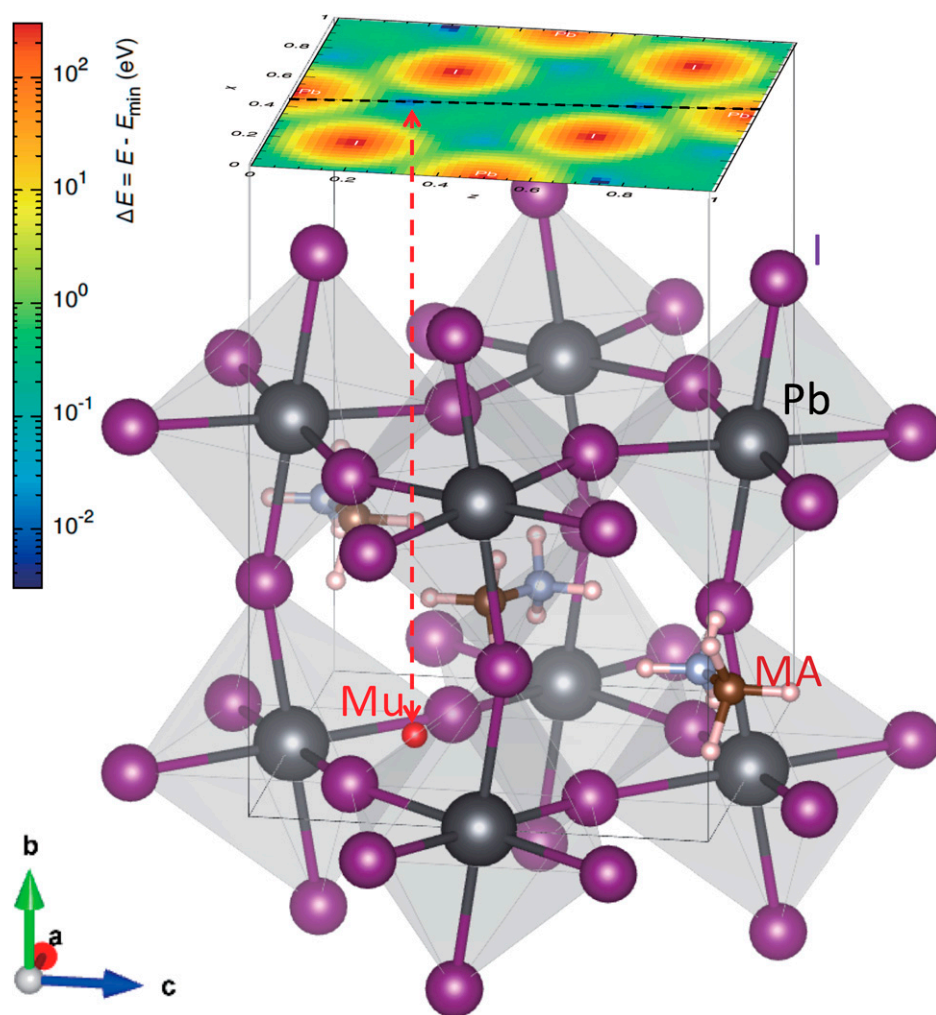
Fig. 1. The crystal structure of $CH_3NH_3PbI_3$ in the orthorhombic phase, where the organic cation (MA) is located in the center of a cage with PbI_6 octahedrons at the corners. It is inferred from μSR and DFT calculations that the implanted muons occupy the (0.48, 0.028, 0.27) site in the unit cell (Mu, marked by a red ball). The color contour map shows the differential total formation energy for an interstitial hydrogen obtained by the DFT calculation.

new materials for a better solar cell performance. It is not easy, however, to experimentally distinguish the two contributions.

A fundamental difference between lattice vibrations and molecular rotations is related to their difference in coherence of dynamics; lattice vibrations are collective in nature with long spatial coherence, while molecular rotations are mainly local and incoherent in space. Thus, a local atomic probe that is sensitive to the molecular dynamics would be most useful, as it can provide information on molecules without relying on the coherence of their dynamics. Muon (Mu, a light isotope of H) spin relaxation technique does just that, as it probes the fluctuation of local magnetic fields at well-defined interstitial sites via Mu spin rotation and relaxation (μSR) experiment. While the quasielastic neutron scattering (15) and NMR/nuclear quadrupole resonance (NMR/NQR; using ^2D and ^{14}N) (17) probe molecular motion over the time scale of 10^{-12} s, μSR provides information over a unique time window of 10^{-9} to 10^{-5} s that may be relevant to the carrier dynamics. In this regard, the fact that NMR using ^{207}Pb and ^{127}I has not been successful so far due to fast relaxation rate ($1/T_2$) further justifies the application of μSR to probe the molecular motion using Mu as a bystander.

Here, we report on the cation molecular dynamics in MAPbI$_3$ revealed by μSR measurements as a function of temperature from 60 K to 360 K. It is known that MAPbI$_3$ undergoes two structural transitions with increasing temperature (18), namely, the orthorhombic-to-tetragonal structural transition at $T_{OT} \simeq$ 162 K, which is followed by the tetragonal-to-cubic transition at $T_{TC} \simeq 327$ K. We show that the μSR time spectra under zero field (ZF)/longitudinal field (LF) can be reasonably reproduced by the dynamical Gaussian Kubo–Toyabe relaxation function, which describes the Mu depolarization by the quasistatic linewidth Δ determined by the random local fields exerted from nuclear magnetic moments and its fluctuation rate ν. Interestingly, a previous μSR study on MAPbI$_3$ reported that the magnitude of Δ exhibits significant variation with temperature in response to the development of cation molecular motion above $\sim$100 K (19), whose microscopic details are yet to be understood. Here, we provide a comprehensive account of how the local motion of cation molecules reduces the contribution of nuclear dipolar fields from ^1H and/or ^{14}N moments by the so-called motional narrowing effect. In addition, we argue that a similar dynamical modulation is in effect for the electric dipole moments associated with methyl ammonium (MA) molecules and that the correlation between the relaxation time of MA molecular motion and the carrier lifetime infers the importance of low-frequency response in the local electric permittivity in the prolonged photo-induced carrier lifetime.

Fig. 2A shows the ZF-μSR time spectra [$A(t)$] observed at typical temperature points in MAPbI$_3$, which is complemented by Fig. 2B showing the overall trend of the spectra versus tem-
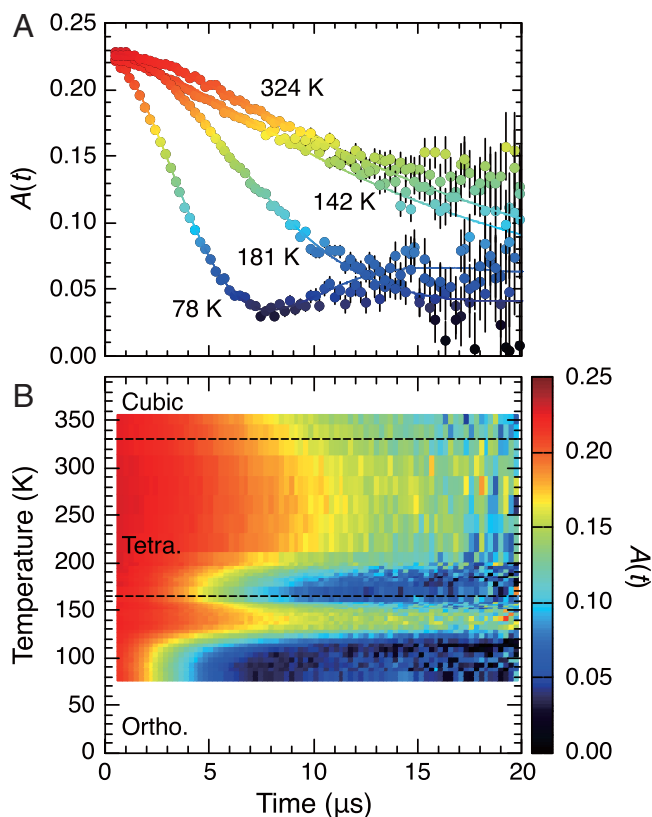
Koda et al.
Organic molecular dynamics and charge-carrier lifetime
in lead iodide perovskite MAPbI$_3$

$$\Delta_r^2 \simeq \gamma_\mu^2 \sum_j \langle B_j^2 \rangle = \gamma_\mu^2 \sum_{j,m} \sum_{\alpha=x,y} \sum_{\beta=x,y,z} \gamma_m^2 (\hat{A}_j I_m)^2,$$

$$\hat{A}_j = A_j^{\alpha\beta} = (3\alpha_j\beta_j - \delta_{\alpha\beta} r_j^2)/r_j^5, \quad (\alpha, \beta = x, y, z), \quad \textbf{[3]}$$

with $\gamma_\mu/2\pi = 135.53$ [MHz/T] being the muon gyromagnetic ratio, $\boldsymbol{r}_j = (x_j, y_j, z_j)$ the position vector of the j-th nucleus (with Mu at the origin), and $\boldsymbol{\mu}_m = \gamma_m \boldsymbol{I}_m$ the nuclear magnetic moment with γ_m being their gyromagnetic ratio. Because ^{14}N and ^{127}I nuclei have spin $I_m \geq 1$, the corresponding $\boldsymbol{\mu}_m$ is subject to electric quadrupolar interaction with the electric field gradient generated by the point charge of the diamagnetic Mu. This leads to the reduction of effective $\boldsymbol{\mu}_m$ to the value parallel with $\boldsymbol{r}_j$ (by a factor $\sqrt{2/3}$ in the classical limit) (20). We also conducted μSR measurements under an LF (B_{LF}) up to 2 mT at each temperature point. The parameters in Eq. **1** (common to the spectra with different B_{LF}) were then determined reliably by simultaneous curve-fits of the spectra at various B_{LF}.

The temperature dependence of Δ deduced from the curve-fits using Eq. **1** is shown in Fig. 3*A*, where Δ exhibits a sharp decrease with increasing temperature above $\Theta_3 \simeq 120$ K and $\Theta_4 \simeq 190$ K across a broad hump around T_{OT}. The corresponding recoveries of asymmetry in the ZF-μSR spectra are also visible in Fig. 2*B*. Meanwhile, no significant change is observed around T_{TC}. It is often presumed that such behavior of Δ is due to the change of Mu sites; we note that λ in Eq. **1** remained small (≤ 0.02 μs^{-1}) throughout the entire temperature range, supporting the negligible ambiguity regarding the temperature dependence of Δ and ν. The Mu position (r) is then estimated by comparing Δ with Δ_r calculated by Eq. **3** for the candidate sites suggested by the DFT calculations; the vicinity of the sites corresponding to the minima of the total formation energy (E_r) for the Mu–MAPbI$_3$ system are examined for the respective structures. The problems associated with the small site occupancy of the MA molecules with varying orientation in the tetragonal and cubic structures are averted by substituting the MA cation with Cs$^+$, which has a nearly equivalent ionic radius ($= 0.18$ nm).

The linewidth Δ_r and differential total energy ΔE_r [$= E_r - E_{r(\min)}$] calculated for three different phases with/without contribution of the MA molecules are shown in Fig. 3*C* along the direction passing the $E_{r(\min)}$ position near the Pb-I basal plane. In the orthorhombic phase, the Mu positions satisfying the condition $\Delta = \Delta_r$ are close to that inferred from $E_{r(\min)}$, which is located near the valley of the electrostatic potential surrounded by negatively charged iodines (the corresponding contour plot for the orthorhombic phase is found in Fig. 1, *Upper*). This indicates that Mu as pseudo-H is in a positively charged state (Mu$^+$). The asymmetric tendency of ΔE_r along the x/z direction is attributed to the broken inversion symmetry of the MA molecules and associated local charge imbalance that leads to the electric dipole moment parallel to the threefold rotational symmetry (C_3) axis. It must be noted that Δ_r is always greater than Δ over the region around $x/z = 0.5$, at which ΔE_r exhibits local minima. Thus, we conclude that the Mu site in this phase is $(0.48, 0.028, 0.27)$, where $\Delta = \Delta_r = 0.230(1)$ μs^{-1}. The estimation for the partially deuterated sample yields $\Delta_r = 0.192$ μs^{-1}, where the reduction can be attributed to the smaller magnetic moment of ^{2}H nuclei.

The Mu sites in the tetragonal ($I4mcm$) and cubic ($Pm\overline{3}m$) phases were also estimated by searching for the position satisfying the condition $\Delta = \Delta_r$ near $\Delta E_{r(\min)}$. As a result, it turned out that Δ_r was always greater than Δ when the contribution from the quasistatic MA molecules was included. This led us to conclude that B_{loc} from the MA cations was reduced by the motional averaging due to the jumping rotation of MA molecules themselves. According to the earlier studies using neutron scattering and NMR/NQR, the jumping rotation of MA molecules around the C_3 axis evolves for $\Theta_3 \leq T \leq T_{OT}$ in the orthorhombic phase, which is followed by the onset of rotation around the

---

Fig. 2. (*A*) Typical examples of ZF-μSR time spectra (μ-e decay asymmetry) observed in MAPbI$_3$ at various temperatures. (*B*) The corresponding contour image of the asymmetry plotted on the time–temperature plane.

perature in a contour plot. These spectra exhibit a slow Gaussian depolarization, which is uniquely attributed to the random local fields from the nuclear magnetic moments. The initial asymmetry [$A_0 = A(0)$] is close to that corresponding to $\sim$100% Mu polarization ($\simeq 0.23$), irrespective of temperature, indicating that muons are mostly in the diamagnetic state (Mu$^+$ or Mu$^-$). Considering that some of the incident muons stop at the backing material (silver), in which the depolarization is negligible, the time spectra are analyzed by curve-fits using the following function:

$$A(t) = A_0 G_{KT}(t; \Delta, \nu) e^{-\lambda t} + A_c, \quad \textbf{[1]}$$

which can be approximated for the case of $\nu \ll \Delta$ and a zero external field by

$$A(t) \simeq A_0 \left[\frac{1}{3} e^{-\nu t} + \frac{2}{3} (1 - \Delta^2 t^2) e^{-\frac{1}{2}\Delta^2 t^2} \right] e^{-\lambda t} + A_c. \quad \textbf{[2]}$$

Here, $G_{KT}(t; \Delta, \nu)$ represents the Gaussian Kubo–Toyabe relaxation function with Δ denoting the linewidth determined by the rms of the corresponding local field distribution and ν being the fluctuation rate of Δ (20). The term $e^{-\lambda t}$ is for the slow residual depolarization of unknown origin (which leads to a slight improvement of fits), and A_c is the background from the Ag sample holder. As shown in Fig. 2*A*, $A(t)$ at 78 K exhibits the characteristic 1/3 term explicit in Eq. **2**, indicating that $\nu \ll \Delta$ at this temperature.

The linewidth Δ is determined by the sum of contributions from the m-th kind of nuclear magnetic moments ($m = 1, 2, 3$, and 4 for ^{1}H, ^{14}N, ^{127}I, and ^{207}Pb, whose natural abundance is nearly 100%),

Koda et al.
Organic molecular dynamics and charge-carrier lifetime
in lead iodide perovskite MAPbI$_3$

PNAS | 3 of 7
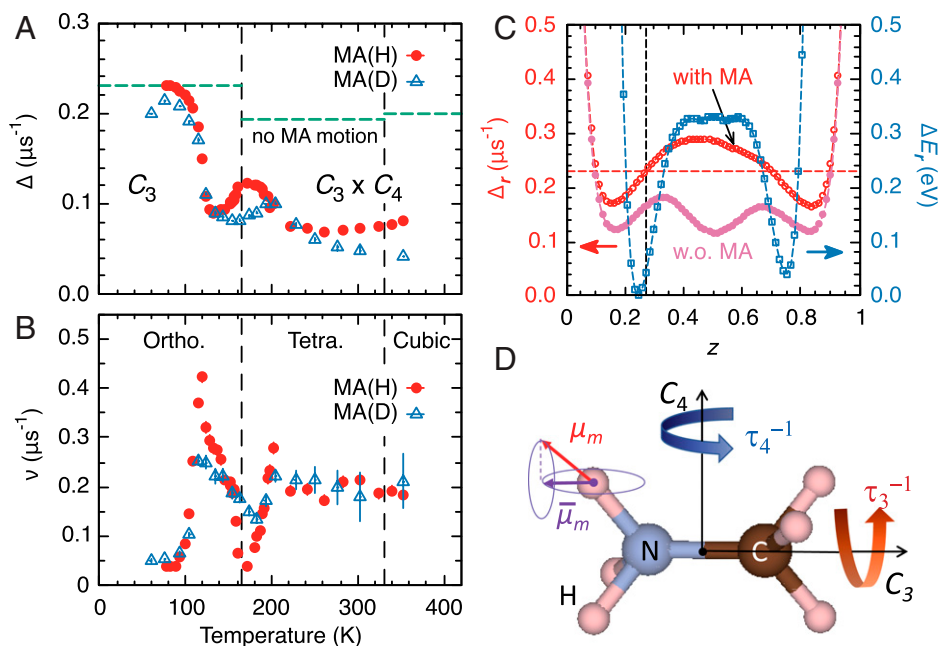https://doi.org/10.1073/pnas.2115812119

Fig. 3. (*A* and *B*) The Kubo–Toyabe linewidth (Δ) (*A*) and fluctuation rate (ν) versus temperature (*B*), where circles and triangles represent data on samples consisting of CH_3NH_3 [MA(H)] and CD_3NH_3 [MA(D)], respectively. Ortho., orthorhombic; tetra., tetragonal. (*C*) The calculated linewidth (Δ_r) versus Mu position (r) in the unit cell, where the z axis is along the path connecting the potential minima shown by the dashed line in the contour plot of Fig. 1. The horizontal dashed line in *C* represents experimental Δ corresponding to the static MA molecules (shown in Table 1), with which the Mu sites are estimated (as marked by vertical lines). The variation of the formation energy (ΔE_r) is also plotted (right axis). The horizontal lines in *A* show Δ_r at the most probable Mu sites without MA molecular motion (also in Table 1). W.o., without. (*D*) Schematic illustrations of the MA molecule with two modes of jumping rotation, where the influence of rotation around the threefold/fourfold symmetry axis (C_i, $i = 3, 4$, with relaxation rate τ_i^{-1}) is illustrated for nuclear magnetic moments (μ_m). The contribution of μ_m to Δ is effectively reduced to $\overline{\mu}_m$ by motional averaging of the nonsecular part around the C_3 axis and then to zero by further averaging around the C_4 axis when $\tau_4^{-1} \gg \Delta$ is satisfied with elevated temperature.

fourfold symmetry (C_4) axis above Θ_4 (15, 17). The relaxation rate of these jumping rotations varies over a range much greater than Δ (i.e., $\tau_{3,4}^{-1} = 10^3$ to 10^6 μs^{-1}) in the relevant temperature range, which is consistent with the fast fluctuation of Δ. As is illustrated in Fig. 3*D*, the rotation around the C_3 axis reduces the contribution of μ_m for ^1H and ^{14}N nuclei to $\overline{\mu}_m$, corresponding to the projection of μ_m to the C_3 axis when $\tau_3^{-1} \gg \Delta$; since the nuclear dipolar fields in Eq. **3** are expressed as

$$B_j = \frac{\mu_m}{r_j^3}[(3\cos^2\theta_r - 1)\cos\theta_m + 3\sin\theta_r\cos\theta_r\sin\theta_m\cos\phi_m],$$
[4]

where θ_r is the polar angle of r_j, θ_m (ϕ_m) are the polar (azimuth) angle of μ_m measured from the C_3 axis, the term proportional to $\sin\theta_m$ in Eq. **4** is averaged out by the jumping rotation ($\langle\cos\phi_m\rangle \simeq 0$) with remaining contribution $\overline{\mu}_m = \mu_m\cos\theta_m$ (20). The contribution is eventually eliminated by further averaging around the C_4 axis ($\perp C_3$) when $\tau_4^{-1} \gg \Delta$, leading to the reduction of the effective Δ in two steps. The small hump of Δ observed around T_{OT} can be interpreted as due to the Mu site change induced by the structural phase transition. This model allowed us to assign the most probable Mu site in the orthorhombic/cubic phases by the condition $\Delta = \Delta_r$ with/without MA contribution for Δ_r. For the tetragonal phase, we adopted the condition that Δ_r without MA contribution was closest to Δ. In Fig. 3*A*, Δ_r for these Mu sites without MA molecular motion is shown for comparison. This allows us to clearly see the effect of MA molecular dynamics on Δ. Table 1 summarizes Δ_r for the candidate Mu sites for the each structural phase.

Provided that the observed decrease in Δ above Θ_3 is mainly due to the jumping rotation of the MA molecules (around the C_3 axis), it is not the whole Δ that is fluctuating, but the local field from the MA molecules. To understand the behavior of ν

shown in Fig. 3*B* in relation to the MA molecular motion [nota bene : ν was obtained by curve-fit analysis using Eq. **1** to allow its arbitrary variation], we phenomenologically extended the Kubo–Toyabe relaxation function to

$$G_{KT}(t; \Delta, \nu) \simeq G_{KT}(t; \Delta_M, \nu_M)\,G_{KT}(t; \Delta_T, \nu_T),$$
[5]

where Δ_M is the nuclear magnetic contributions from the MA molecules, Δ_T [$= (\Delta^2 - \Delta_M^2)^{1/2}$] is the remaining quasistatic part, and ν_M and ν_T are the corresponding fluctuation frequencies of Δ_T and Δ_M. Considering that $\nu_T \ll \Delta_T$ at low temperatures, we have

$$G_{KT}(t; \Delta, \nu) \simeq \frac{1}{3}e^{-\nu_M t} + \frac{2}{3}[1 - \Delta_T^2 t^2 + \frac{\Delta_M^2}{\nu_M}(e^{-\nu_M t} - 1)t]\,G_x(t),$$
[6]

Table 1. The Kubo–Toyabe linewidth (Δ_r) calculated for the most probable Mu sites in the respective structural phases of MAPbI$_3$ with a variety of *A* cations

	Δ_r, μs^{-1}		
A cation	Orthorhombic	Tetragonal	Cubic
CH_3NH_3	0.2302	0.1934	0.1989
C–N	0.1656	0.0948	0.0814
Null	0.1455	0.0946	0.0812
CD_3NH_3	0.1920	0.1542	0.1328
Δ (exp.)	0.2298(8) [78 K]	0.1218(5) [171 K]	0.0813(9) [352 K]
	0.091(1) [133 K]	0.0679(7) [260 K]	
Mu site	(0.48, 0.028, 0.27)	(0.54, 0.044, 0)	(0.58, 0.58, 0)

The lower rows are for Δ observed as extreme values (Fig. 3*A*) and atomic coordinates of the assigned Mu sites.

Koda et al.
Organic molecular dynamics and charge-carrier lifetime
in lead iodide perovskite MAPbI$_3$

where $G_x(t)$ is the relaxation function under a transverse field (20, 21),

$$G_x(t) = e^{-\frac{1}{2}\Delta_T^2 t^2} \exp[-\frac{\Delta_M^2}{\nu_M^2}(e^{-\nu_M t} - 1 + \nu_M t)], \quad [7]$$

which is exact for any ν_M. Then, in the case of $\nu_M \ll \Delta_T, \Delta_M$, we have

$$G_{KT}(t;\Delta,\nu) \simeq \frac{1}{3}e^{-\nu_M t} + \frac{2}{3}[1 - \Delta^2 t^2]e^{-\frac{1}{2}\Delta^2 t^2}. \quad [8]$$

Therefore, the value of ν obtained from the fit by Eq. 1 corresponds to ν_M. On the other hand, if $\nu_M \gtrsim \Delta_M$, Eq. 5 can be roughly approximated to yield

$$G_{KT}(t;\Delta,\nu) \simeq G_{KT}(t;\Delta_T,0)e^{-\frac{\Delta_M^2}{\nu_M}t}, \quad [9]$$

and the apparent decrease of ν obtained by fitting with Eq. 1 can be attributed to the increase of ν_M, because ν as a fitting parameter is proportional to Δ_M^2/ν_M. Thus, the behavior in ν seen for $\Theta_3 \leq T \leq T_{OT}$ in Fig. 3B can be interpreted as that due to the increase in the jump rotation frequency of the MA molecule around the C_3 axis.

The change in ν for $\Theta_4 \leq T \leq 220$ K is also attributed to the similar mechanism acting on Δ_T due to the increase of jumping rate around the C_4 axis, where Δ_M and Δ_T in Eq. 5 are replaced by $\Delta_{\overline{M}}$ (the remaining contribution from the MA molecules) and by Δ_L [$= (\Delta_T^2 - \Delta_{\overline{M}}^2)^{1/2}$, consisting only of the PbI$_3$ lattice contribution] with their fluctuation rate $\nu_{\overline{M}}$ and ν_L, respectively. The increase of ν for $T_{OT} \leq T \leq 200$ K is then understood as that of $\nu_{\overline{M}}$, and the turnover above $\sim$200 K is described by $\nu \propto \Delta_{\overline{M}}^2/\nu_{\overline{M}}$. The residual value of $\nu \simeq \nu_L \simeq 0.2$ μs^{-1} at higher temperatures is attributed to the diffusion of iodine ions in the relevant temperature range (19, 22).

The variation of Δ in the tetragonal phase can be used to evaluate the reduction factor $x = \overline{\mu}_m/\mu_m$ by the motional effect using the relation

$$\Delta_T^2 = \Delta_L^2 + x^2(\Delta - \Delta_L^2). \quad [10]$$

Assuming that $\Delta = 0.1934$ μs^{-1} (calculated for the tetragonal phase), $\Delta_T = 0.1218(5)$ μs^{-1} (at 171 K), and $\Delta_L = 0.0679(7)$ (at 260 K, which is close enough to $\Delta_r = 0.0946$ μs^{-1} calculated without MA molecules), we have $x = 0.56(3)$. Meanwhile, the amount of change in Δ between 78 K and $\sim$133 K [$= 0.090(1)$ μs^{-1}] in the orthorhombic phase exceeds that predicted by quenching the contribution of MA molecules, which we tentatively attribute to the additional motion of Mu itself induced by the evolution of the relatively slow MA jumping rotation around the C_4 axis ($10^0 \lesssim \nu \lesssim 10^2$ μs^{-1}; not susceptible for neutron/NMR). As shown in Fig. 3C, the potential energy for Mu is asymmetric along the C_3 axis, and Mu tends to stay near the CH$_3$ bases. The fluctuation of the Mu potential induced by the MA reorientation around the C_4 axis will activate the Mu hopping between the equivalent sites in the unit cell, leading to the fluctuation of Δ_L. Note that this motion does not affect the averaging of Δ around the C_3 axis.

It is remarkable that the overall temperature dependence of Δ, including the hump around T_{OT}, is in close resemblance with that observed for the photoluminescence (PL) lifetime (16). As shown in Fig. 4A, the longer lifetime (τ_{PL1}) exhibits a sharp decrease above Θ_3, which is followed by a small hump around T_{OT} and the further reduction above Θ_4. A similar trend is observed for the shorter lifetime (τ_{PL2}). Moreover, it is obvious in Fig. 4B that these behaviors are in parallel with the steep reduction of τ_3 and subsequent onset and reduction of τ_4 with increasing temperature. Such correlations suggest an intrinsic relationship between the lifetime of photoexcited carriers and the MA molecular motion, which can be understood by considering that the mechanism causing the change in Δ is also in effect for
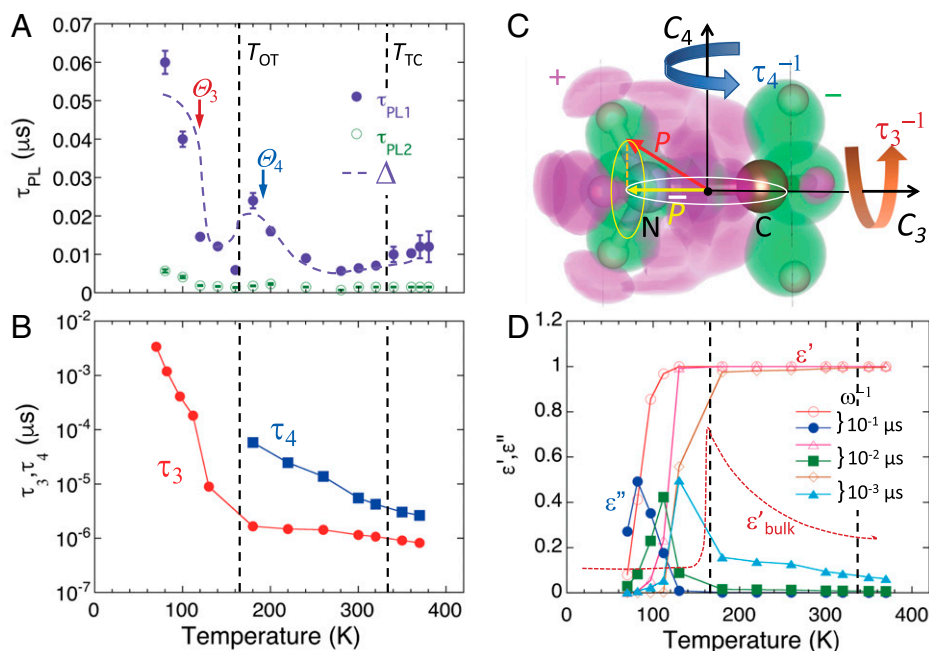
Fig. 4. (A) PL lifetime versus temperature in MAPbI$_3$ (quoted from ref. 16), where the dashed curve indicates Δ (^{1}H) versus temperature shown in Fig. 3A. (B) The relaxation time τ_3 (τ_4) (in logarithmic scale) of the rotational motion around the C_3 (C_4) axis determined by quasielastic neutron scattering (after ref. 15). (C) Schematic illustrations of the MA molecule with two modes of jumping rotation, where the hatched areas indicate the local charge asymmetry obtained by the DFT calculation. (D) The contribution of MA molecules to the complex permittivity [$\varepsilon(\omega) = \varepsilon' + i\varepsilon''$] estimated by the Debye model (see Eqs. 11 and 12 in text). The symbols in D are predicted behavior of $\varepsilon(\omega)$ when ω^{-1} is near the PL lifetime. ε'_{bulk} is the bulk permittivity (after ref. 23).

Koda et al.
Organic molecular dynamics and charge-carrier lifetime
in lead iodide perovskite MAPbI$_3$

PNAS | 5 of 7
https://doi.org/10.1073/pnas.2115812119

the local dielectric permittivity $\varepsilon(\omega)$. As is illustrated in Fig. 4C, the MA molecule has an electric dipole moment $\boldsymbol{P}$ along the C_3 axis due to the local charge imbalance, whose effective value seen from photoexited carriers is subject to reduction by the motional averaging on a certain time scale; it is reduced to $\overline{\boldsymbol{P}}$ (a projection to the C_3 axis) by jumping rotation around the C_3 axis, then to zero by additional rotation around C_4.

Here, let us consider the contribution of the MA molecules using the Debye model (24) in order to discuss the relationship with the dielectric permittivity in more detail. The dielectric response of noninteracting dipoles is described by the complex permittivity $\varepsilon(\omega) = \varepsilon'(\omega) + i\varepsilon''(\omega)$ with

$$\varepsilon'(\omega) = \varepsilon_\infty + (\varepsilon_s - \varepsilon_\infty)\frac{1}{1 + \omega^2\tau^2}, \qquad \textbf{[11]}$$

$$\varepsilon''(\omega) = (\varepsilon_s - \varepsilon_\infty)\frac{\omega\tau}{1 + \omega^2\tau^2}, \qquad \textbf{[12]}$$

where ε_s $[= \varepsilon(0)]$ is the static permittivity, $\varepsilon_\infty = \varepsilon(\infty)$, and τ is the relaxation time of the electric dipoles. We assume that τ for the MA molecules is determined by the mean value $\tau_{MA}^{-1} = \tau_3^{-1} + \tau_4^{-1}$. While $\varepsilon_s - \varepsilon_\infty \simeq N|\boldsymbol{P}|^2/3k_B T$ for the free dipoles (with N being the number of dipoles in the unit volume), we presume that the temperature dependence for the MA molecules is represented by that of τ_{MA} via τ_i shown in Fig. 4B. Assuming that $\varepsilon_\infty = 0$, the calculated ε' and ε'' (normalized by ε_s) versus temperature is shown in Fig. 4D for a variety of ω^{-1} relevant with τ_{PLi}. The coincidence between Θ_3 and the temperature where $\varepsilon''(\omega)$ exhibits a peak observed for $\omega \sim 10^2$ μs^{-1} suggests that the inelastic (energy exchanging) interaction between the photoinduced carriers and MA cations in this frequency range is a crucial factor in determining the carrier lifetime. Such a low-frequency response is expected to help reorienting MA molecules in response to the Coulomb interaction with carriers, serving as an electric screening due to the local permittivity. Meanwhile, the static component (ε') shows the least dependence on temperature [$\varepsilon'(\omega) \simeq \varepsilon_s$ for $\omega \leq 10^3$ μs^{-1}], contributing to the bulk static permittivity (ε'_{bulk}) as a constant offset. The Curie–Weiss behavior of ε'_{bulk} reported in the literature (23) is then attributed to the translational displacement of MA molecules against the Pb-I lattice, where the displacement is unlocked by the onset of the fast jumping rotation around the C_4 axis.

Finally, as inferred from the temperature dependence of Δ and τ_3, the characteristic temperature (Θ_3) where the MA molecular motion exhibits sharp enhancement is significantly lower than T_{OT}. Within the above scenario, this suggests that the structural phase transition is driven by the MA molecular motion (25), which is in line with the shift of the hump in Δ to a higher temperature ($\sim$200 K) for the deuterated MA, in which a higher T_{OT} is also inferred from the previous diffraction study (26). The similar situation is then speculated for the tetragonal-to-cubic transition, which may be important to consider the relative stability of the PbI_3 frame structure.

In conclusion, our detailed μSR study on MAPbI$_3$ that is a local probe as a function of T clearly shows that the molecular rotations make the major contribution to the formation of large polarons and thus to the long carrier lifetime in the HOIP.

Materials and Methods

The conventional μSR measurements were carried out on two types of powder samples, one consisting of pristine MA and another partially substituted by deuterium (i.e., $CD_3NH_3^+$). The sample packed in aluminum foil was mounted on a silver sample holder, which was attached to an He-flow cryostat for varying temperature over a range from 60 K through 360 K. The time evolution of the Mu spin polarization was monitored by measuring the μ-e decay asymmetry, $A(t)$, using the ARTEMIS spectrometer furnished at the S1 area of the Japan Proton Accelerator Research Complex (J-PARC) Muon Science Establishment, Japan. The DFT calculations were performed by using the projector-augmented wave approach (27) implemented in the Vienna ab initio simulation package (28) with the Perdew–Burke–Ernzerhof exchange-correlation potential (29), where the lattice parameters reported in the literature were adopted (18). The cutoff energy for the plane-wave basis set was 400 eV. The distribution of the local magnetic field at the Mu sites was calculated by using the Dipelec program (30). The crystal structures were visualized by using the VESTA program (31).

Data Availability. All study data are included in the article.

1. A. Kojima, K. Teshima, Y. Shirai, T. Miyasaka, Organometal halide perovskites as visible-light sensitizers for photovoltaic cells. *J. Am. Chem. Soc.* **131**, 6050–6051 (2009).
2. G. Kim *et al.*, Impact of strain relaxation on performance of α-formamidinium lead iodide perovskite solar cells. *Science* **370**, 108–112 (2020).
3. J. Yang, T. L. Kelly, Decomposition and cell failure mechanisms in lead halide perovskite solar cells. *Inorg. Chem.* **56**, 92–101 (2017).
4. W. Ke *et al.*, Enhanced photovoltaic performance and stability with a new type of hollow 3D perovskite enFASnI$_3$. *Sci. Adv.* **3**, e1701293 (2017).
5. S. Shao *et al.*, Highly reproducible sn-based hybrid perovskite solar cells with 9% efficiency. *Adv. Energy Mater.* **8**, 1702019 (2018).
6. T. M. Brenner, D. A. Egger, L. Kronik, G. Hodes, D. Cahen, Hybrid organic—inorganic perovskites: Low-cost semiconductors with intriguing charge-transport properties. *Nat. Rev. Mater.* **1**, 15007 (2016).
7. J. M. Frost *et al.*, Atomistic origins of high-performance in hybrid halide perovskite solar cells. *Nano Lett.* **14**, 2584–2590 (2014).
8. Y. Kutes *et al.*, Direct observation of ferroelectric domains in solution-processed CH$_3$NH$_3$PbI$_3$ perovskite thin films. *J. Phys. Chem. Lett.* **5**, 3335–3339 (2014).
9. E. Strelcov *et al.*, CH$_3$NH$_3$PbI$_3$ perovskites: Ferroelasticity revealed. *Sci. Adv.* **3**, e1602165 (2017).
10. F. Zheng, L. Z. Tan, S. Liu, A. M. Rappe, Rashba spin–orbit coupling enhanced carrier lifetime in CH$_3$NH$_3$PbI$_3$. *Nano Lett.* **15**, 7794–7800 (2015).
11. T. Etienne, E. Mosconi, F. De Angelis, Dynamical origin of the Rashba effect in organohalide lead perovskites: A key to suppressed carrier recombination in perovskite solar cells? *J. Phys. Chem. Lett.* **7**, 1638–1645 (2016).
12. Y. Yamada, M. Hoyano, R. Akashi, K. Oto, Y. Kanemitsu, Impact of chemical doping on optical responses in bismuth-doped CH$_3$NH$_3$PbBr$_3$ single crystals: Carrier lifetime and photon recycling. *J. Phys. Chem. Lett.* **8**, 5798–5803 (2017).
13. Y. Chen *et al.*, Extended carrier lifetimes and diffusion in hybrid perovskites revealed by Hall effect and photoconductivity measurements. *Nat. Commun.* **7**, 12253 (2016).
14. H. Zhu *et al.*, Screening in crystalline liquids protects energetic carriers in hybrid perovskites. *Science* **353**, 1409–1413 (2016).
15. T. Chen *et al.*, Rotational dynamics of organic cations in the CH$_3$NH$_3$PbI$_3$ perovskite. *Phys. Chem. Chem. Phys.* **17**, 31278–31286 (2015).
16. T. Chen *et al.*, Origin of long lifetime of band-edge charge carriers in organic-inorganic lead iodide perovskites. *Proc. Natl. Acad. Sci. U.S.A.* **114**, 7519–7524 (2017).
17. G. M. Bernard *et al.*, Methylammonium cation dynamics in methylammonium lead halide perovskites: A solid-state NMR perspective. *J. Phys. Chem. A* **122**, 1560–1573 (2018).
18. M. T. Weller, O. J. Weber, P. F. Henry, A. M. Di Pumpo, T. C. Hansen, Complete structure and cation orientation in the perovskite photovoltaic methylammonium lead iodide between 100 and 352 K. *Chem. Commun. (Camb.)* **51**, 4180–4183 (2015).
19. D. W. Ferdani *et al.*, Partial cation substitution reduces iodide ion transport in lead iodide perovskite solar cells. *Energy Environ. Sci.* **12**, 2264–2272 (2019).
20. R. S. Hayano *et al.*, Zero-and low-field spin relaxation studied by positive muons. *Phys. Rev. B Condens. Matter* **20**, 850–859 (1979).
21. R. Kubo, K. Tomita, A general theory of magnetic resonance absorption. *J. Phys. Soc. Jpn.* **9**, 888–919 (1954).
22. R. García-Rodríguez, D. Ferdani, S. Pering, P. J. Baker, P. J. Cameron, Influence of bromide content on iodide migration in inverted MAPb(I$_{1-x}$Br$_x$)$_3$ perovskite solar cells. *J. Mater. Chem. A Mater. Energy Sustain.* **7**, 22604–22614 (2019).

6 of 7 | **PNAS**
https://doi.org/10.1073/pnas.2115812119

Koda et al.
Organic molecular dynamics and charge-carrier lifetime
in lead iodide perovskite MAPbI$_3$

23. N. Onoda-Yamamuro, T. Matsuo, H. Suga, Dielectric study of $CH_3NH_3PbX_3$ (X = Cl, Br, I). *J. Phys. Chem. Solids* **53**, 935–939 (1992).

24. P. Debye, *Polar Molecules* (Dover Publications, New York, 1929).

25. T. Chen *et al.*, Entropy-driven structural transition and kinetic trapping in formamidinium lead iodide perovskite. *Sci. Adv.* **2**, e1601650 (2016).

26. P. S. Whitfield *et al.*, Structures, phase transitions and tricritical behavior of the hybrid perovskite methyl ammonium lead iodide. *Sci. Rep.* **6**, 35685 (2016).

27. G. Kresse, D. Joubert, From ultrasoft pseudopotentials to the projector augmented-wave method. *Phys. Rev. B Condens. Matter Mater. Phys.* **59**, 1758–1775 (1999).

28. G. Kresse, J. Furthmüller, Efficient iterative schemes for ab initio total-energy calculations using a plane-wave basis set. *Phys. Rev. B Condens. Matter* **54**, 11169–11186 (1996).

29. J. P. Perdew, K. Burke, M. Ernzerhof, Generalized gradient approximation made simple. *Phys. Rev. Lett.* **77**, 3865–3868 (1996).

30. K. M. Kojima *et al.*, Site-dilution in the quasi-one-dimensional antiferromagnet $Sr_2(Cu_{1-x}Pd_x)O_3$: Reduction of Néel temperature and spatial distribution of ordered moment sizes. *Phys. Rev. B Condens. Matter Mater. Phys.* **70**, 094402 (2004).

31. K. Momma, F. Izumi, *VESTA3* for three-dimensional visualization of crystal, volumetric and morphology data. *J. Appl. Cryst.* **44**, 1272–1276 (2011).

Koda et al.
Organic molecular dynamics and charge-carrier lifetime
in lead iodide perovskite MAPbI$_3$

PNAS | 7 of 7
https://doi.org/10.1073/pnas.2115812119